This journal is © the Owner Societies 2009

Supporting Information for

Radiofrequency Polarisation Effects in Zero-Field Electron Paramagnetic Resonance

by Christopher T. Rodgers, C. J. Wedge, Stuart A. Norman, P. Kukura, K. Nelson, N. Baker, Kiminori Maeda, K. B. Henbest, P. J. Hore and C. R. Timmel.

S1 Further theoretical considerations

In the main text, we presented theoretical (Figs. 1–3, Eq. 5) and experimental evidence that weak CP and LP radiofrequency excitations produce quite distinct zero-field EPR spectra. Here, we provide further theoretical insights into the physical origin of these effects.

S1.1 Eigenvalues of the Hamiltonian

The fundamental differences between the effects of CP and LP radiofrequency fields may be seen by inspection of the eigenvalues of the Hamiltonian of a one-proton radical pair. The Hamiltonian for a radical pair containing just one spin-½ nucleus in one of the radicals is

$$\hat{H}_{\mathrm{LP}}(t) = a\hat{\boldsymbol{I}}\cdot\hat{\boldsymbol{S}}_{\mathrm{A}} + \omega_1\sqrt{2}\cos\left(\omega_{\mathrm{rf}}t+\gamma\right)\left(\hat{S}_{\mathrm{A}x}+\hat{S}_{\mathrm{B}x}\right) \tag{S1}$$

in the presence of a LP radiofrequency field, and

$$\begin{aligned}\hat{H}_{\mathrm{CP}}(t) = a\hat{\boldsymbol{I}}\cdot\hat{\boldsymbol{S}}_{\mathrm{A}} &+ \omega_1\cos\left(\omega_{\mathrm{rf}}t+\gamma\right)\left(\hat{S}_{\mathrm{A}x}+\hat{S}_{\mathrm{B}x}\right)\\ &\pm\omega_1\sin\left(\omega_{\mathrm{rf}}t+\gamma\right)\left(\hat{S}_{\mathrm{A}y}+\hat{S}_{\mathrm{B}y}\right)\end{aligned} \tag{S2}$$

for a CP field.

It is most informative to compare systems with the same root-mean-squared (RMS) field strength $B_1 = -\omega_1/\gamma_{\mathrm{e}}$, as done in the main text. Thus, writing electron and nuclear spin operators explicitly in the product basis, we expand the Hamiltonians above to give 8×8 real, symmetric matrices, whose eigenvalues are

LP	**CP**
$\frac{a}{4}$ (twice)	$\frac{a}{4}$ (twice)
$\frac{a}{4}\pm\sqrt{2}\omega_1 c$	$\frac{a}{4}\pm\omega_1$
$\frac{1}{4}\left(-a\pm 2\sqrt{2}\omega_1 c\pm 2\sqrt{a^2+2\omega_1^2c^2}\right)$	$\frac{1}{4}\left(-a\pm 2\sqrt{a^2+2\omega_1^2\pm 2\omega_1\sqrt{a^2+\omega_1^2}}\right)$.

The $\pm$ combinations in the final row should be taken independently to give four eigenvalues and $c=\cos\left(\omega_{\mathrm{rf}}t+\gamma\right)$.

Although the eigenvalues for CP and LP radiation appear similar, there is a critical difference: only the LP eigenvalues depend on time, whereas those in the CP case are time-independent. Physically, this corresponds to the fact that the strength of a CP field does not depend on time, whereas that of a LP field is time-dependent.

S1.2 Rotating frame transformation

Since the earliest days of the theory of NMR, the rotating frame transformation (RFT) has been used in suitable systems to convert a time-dependent Hamiltonian $\hat{H}(t)$ written in the laboratory co-ordinate system into a time-independent Hamiltonian $\hat{H}'$. This is advantageous because it is much simpler to calculate the spin dynamics in a system with a time-independent Hamiltonian.

The transformation is often explained pictorially in terms of classical mechanics. For example, in high field NMR, the RFT switches to a co-ordinate system that rotates about the static magnetic field B_0 at the Larmor frequency (see [1] for details). In this rotating co-ordinate system, the Hamiltonian for a single nuclear spin exposed to a resonant RF field becomes time-independent.

For our purposes, we must express the RFT in the quantum mechanical formalism used to calculate magnetic field effects. The RFT amounts to a change of basis states from a normal time-independent basis such as the product basis to a cleverly chosen set of time-dependent basis states. In favourable cases, the transformation succeeds in shifting all of the time-dependence from the Hamiltonian into the definition of the basis states.

Following [2, 3], we consider a radical pair subject to orthogonal static and circularly polarized RF fields. Its time-dependent Hamiltonian is written

$$\hat{H}(t;\gamma) = \sum_{N=\mathrm{A}}^{\mathrm{B}} \sum_{i} a_{Ni}\hat{\boldsymbol{I}}_{Ni}\cdot\hat{\boldsymbol{S}}_N + \omega_0\hat{S}_{Nz} + \omega_1\sqrt{\frac{1}{2}}\begin{bmatrix} \left(\hat{S}_{Nx}-\hat{S}_{Ny}\right)\cos\left(\omega_{\mathrm{rf}}t+\gamma\right) \\ +\left(\hat{S}_{Nx}+\hat{S}_{Ny}\right)\sin\left(\omega_{\mathrm{rf}}t+\gamma\right)\end{bmatrix}. \tag{S3}$$

The wave function $|\psi\rangle(t)$ for a pure state in the laboratory co-ordinate system evolves according to the Schrödinger equation:

$$\frac{\partial|\psi\rangle(t)}{\partial t} = -\mathrm{i}\hat{H}(t;\gamma)|\psi\rangle(t). \tag{S4}$$

The RFT produces a new set of wave functions $|\phi\rangle(t) = T(t)|\psi\rangle(t)$, where $T(t)$ is a time-dependent unitary transformation matrix. Differentiating this expression, we write

$$\frac{\partial|\phi\rangle(t)}{\partial t} = \frac{\partial T(t)}{\partial t}|\psi\rangle(t) + T(t)\frac{\partial|\psi\rangle(t)}{\partial t}. \tag{S5}$$

Using equation (S4) and the fact that $|\psi\rangle(t) = T^{\dagger}(t)\,|\phi\rangle(t)$, we write

$$\begin{aligned}\frac{\partial\,|\phi\rangle(t)}{\partial t} &= \left[\frac{\partial T(t)}{\partial t} - \mathrm{i}T(t)\hat{H}(t;\gamma)\right]|\psi\rangle(t)\\ &= -\mathrm{i}\underbrace{\left[\mathrm{i}\frac{\partial T(t)}{\partial t}T^{\dagger}(t) + T(t)\hat{H}(t;\gamma)T^{\dagger}(t)\right]}_{\hat{H}'}|\phi\rangle(t).\end{aligned} \tag{S6}$$

This equation for the evolution of the rotating frame wave functions $|\phi\rangle(t)$ is identical in form to the Schrödinger equation if we identify the bracketed quantity as an effective rotating frame Hamiltonian $\hat{H}'$. As shown in Appendix A, the rotating frame Hamiltonian for a radical pair does not depend on time if we choose the transformation operator

$$T(t) = \exp\left(\mathrm{i}\omega_{\mathrm{rf}}t\sum_{N=\mathrm{A}}^{\mathrm{B}}\left[\hat{S}_{Nz} + \sum_i \hat{I}_{Niz}\right]\right). \tag{S7}$$

Since spin operators for different spins commute, we may write this as

$$T(t) = \prod_j \exp\left(\mathrm{i}\hat{L}_{jz}\omega_{\mathrm{rf}}t\right), \tag{S8}$$

where the product is taken over all electron and nuclear spins $\hat{\boldsymbol{L}}_j$ in the radical pair.

S1.3 Rotating frame approximation

In high field NMR, the RF fields applied by the spectrometer probe are typically linearly polarized. Similarly, in high field EPR, the microwaves applied to the sample are linearly polarized. Yet linearly polarized fields such as these may be considered to be the superposition of two *notional* circularly polarized fields. For example, we may write a linearly polarized field of RMS RF field strength $B_1 = -\omega_1/\gamma_{\mathrm{e}}$ as

$$\boldsymbol{B}_{\mathrm{LP}}(t) = \boldsymbol{i}\sqrt{2}\omega_1\cos\omega_{\mathrm{rf}}t = \tilde{\boldsymbol{B}}_{\mathrm{CP}+}(t) + \tilde{\boldsymbol{B}}_{\mathrm{CP}-}(t), \tag{S9}$$

where the notional circularly polarized fields are

$$\tilde{\boldsymbol{B}}_{\mathrm{CP}\pm}(t) = \boldsymbol{i}\sqrt{\frac{1}{2}}\omega_1\cos\omega_{\mathrm{rf}}t \pm \boldsymbol{j}\sqrt{\frac{1}{2}}\omega_1\sin\omega_{\mathrm{rf}}t \tag{S10}$$

and $\boldsymbol{i}$ and $\boldsymbol{j}$ are the unit vectors along the x- and y-axes respectively. Notice that each notional circularly polarized RF field has RMS strength $B_1^{\diamond} = B_1/\sqrt{2}$.

The RFT outlined above is not capable of eliminating the time-dependence of the Hamiltonian exactly for a system under the influence of $\boldsymbol{B}_{\mathrm{LP}}(t)$. However, when the radiofrequency ν_{rf} is close to resonance, the $\tilde{\boldsymbol{B}}_{\mathrm{CP}+}(t)$ component satisfies the Zeeman resonance condition, whilst the $\tilde{\boldsymbol{B}}_{\mathrm{CP}-}(t)$

component is $\sim 2\nu_{\mathrm{rf}}$ away from resonance. In high field NMR and EPR, this is significantly more than the linewidth and hence it is an excellent approximation to neglect the effects of the $\tilde{\boldsymbol{B}}_{\mathrm{CP}-}(t)$ component of the RF field. It is then quite possible to calculate the effects of the $\tilde{\boldsymbol{B}}_{\mathrm{CP}+}(t)$ component alone using the RFT outlined above. Neglecting the effects of the $\tilde{\boldsymbol{B}}_{\mathrm{CP}-}(t)$ component of a linearly polarized RF field is known as the "rotating frame approximation" [4–9]. The rotating frame approximation is extremely well-attested experimentally at high fields, giving excellent agreement with measured signals.

The situation is more complex when there is no static field, *i.e.* $B_0 = 0$, as in our experiments. The $\tilde{\boldsymbol{B}}_{\mathrm{CP}-}(t)$ component is no longer off resonance, and hence the rotating frame approximation will break down.

S1.4 Relationship to present experiments

The significance of the time-dependence of the radical pair Hamiltonian eigenvalues given in equations (S1) and (S2) may now be exposed. Expanding the radical pair Hamiltonian in terms of its eigenvectors and eigenvalues, we write

$$\hat{H}_{\mathrm{LP}}(t) = X_{\mathrm{LP}}(t)\Lambda_{\mathrm{LP}}(t)X_{\mathrm{LP}}^{\dagger}(t) \tag{S11}$$

$$\hat{H}_{\mathrm{CP}}(t) = X_{\mathrm{CP}}(t)\Lambda_{\mathrm{CP}}X_{\mathrm{CP}}^{\dagger}(t) \tag{S12}$$

where X is the unitary matrix of eigenvectors and Λ is the diagonal matrix of eigenvalues of $\hat{H}$.

Suppose in the CP case that there exists a time-dependent unitary matrix $T(t)$ such that

$$T(t)X_{\mathrm{CP}}(t) = Y_{\mathrm{CP}}, \tag{S13}$$

where Y_{CP} does not depend on time. Then, the quantity

$$T(t)\hat{H}_{\mathrm{CP}}(t)T^{\dagger}(t) = Y_{\mathrm{CP}}\Lambda_{\mathrm{CP}}Y_{\mathrm{CP}}^{\dagger} \tag{S14}$$

will not depend on time. Following the derivation for the rotating frame transformation given above, we see that providing the "Coriolis" term $\frac{\partial T(t)}{\partial t}T^{\dagger}(t)$, discussed in Appendix A.5, also does not depend on time, we can make a change of basis to produce a time-independent effective Hamiltonian. The rotating frame transformation typically applied in high field NMR and EPR arises from one such choice of time-dependent unitary transformation $T(t)$.

Unfortunately, in the LP case, even if there exists an equivalent unitary matrix $T(t)$ then the quantity

$$T(t)\hat{H}_{\mathrm{LP}}T^{\dagger}(t) = Y_{\mathrm{LP}}\Lambda_{\mathrm{LP}}(t)Y_{\mathrm{LP}}^{\dagger} \tag{S15}$$

is still time-dependent because of the time-dependence of the eigenvalues $\Lambda_{\mathrm{LP}}(t)$. Except in very

special cases where the "Coriolis" term exactly counteracts this time dependence, equation (S15) means that the Hamiltonian for a LP field is inherently time-dependent and that this time dependence cannot be removed by a unitary transformation (*i.e.* by a change of basis). Therefore, not only does the rotating frame transformation not hold for LP fields, but there is no possibility to find an analogous transformation either.

S1.5 Limit of weak radiofrequency fields

Figure S1 shows the simulated product yield of a radical pair containing a single spin-½ nucleus in the limit of very weak LP and CP polarized radiofrequency fields so that $\omega_1 \ll a$. (This is analogous to Figure 1 in the main paper). It can be seen that very weak LP and CP fields of the same RMS field

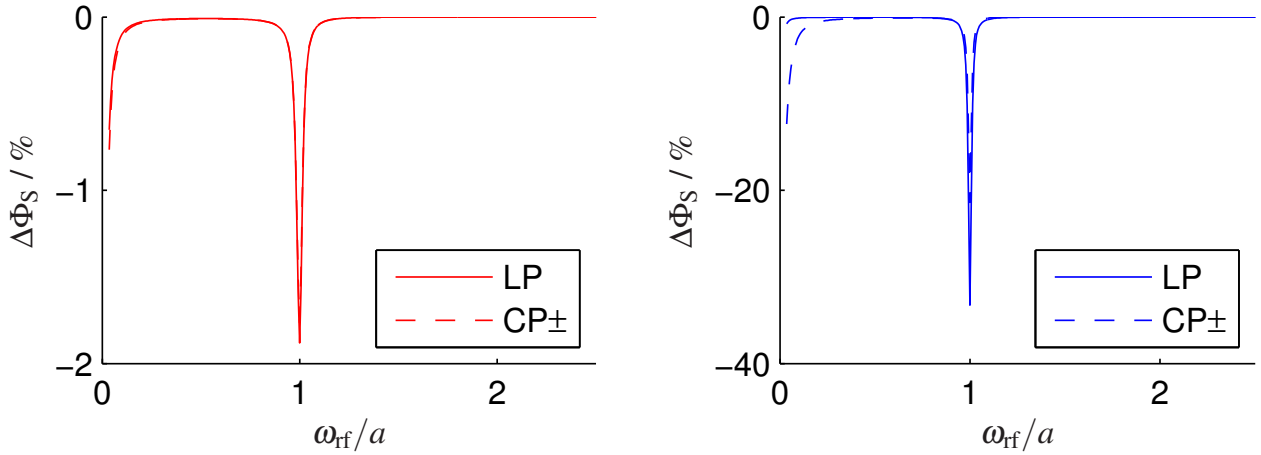

(a) $2\pi k = a/10$ (b) $2\pi k = a/100$

Figure S1: Simulations showing the influence of a radiofrequency field of angular frequency ω_{rf} and RMS amplitude $B_1 = a/100$ on the singlet product yield of a radical pair reaction. The spectra were calculated for radical pairs containing a single spin-½ nucleus, with a hyperfine coupling constant a and recombination rate constant k. Polarizations of the radiofrequency fields are shown in the legend. The vertical axis shows the percentage change in the singlet yield produced by the radiofrequency field. CP+ and CP− have identical effects.

strength produce identical effects. Indeed, in the absence of any radiofrequency fields, *i.e.* in the limit $\omega_1 \to 0$, $\hat{H}_{LP} = \hat{H}_{CP}$, so there could be no "polarization effect" without an RF field. Since the RP Hamiltonian is differentiable with respect to RF field strength, one could envisage all the resulting properties as a Taylor series in B_1. This series would have no constant term, and would be unlikely to have large higher order terms. It seems quite plausible, therefore, that the polarization effect of a weak RF field should be small.

S1.6 Effect of initial RF phase

Figure 3 in the main text displays the time dependence of the singlet probability of a one-proton radical pair with $a = 1\,\mathrm{mT}$ in the presence of either a CP or LP radiofrequency field (strength $B_1 =$

100 μT) or with no field at all. That figure shows clearly that both CP and LP fields affect the spin evolution of the radical pair, but that they do so differently.

In Figure 3, the effects of a LP field were summarised by averaging over the initial phase of the radiofrequency field γ. Figure S2 shows the time-dependence of the change in singlet probability caused by a LP field for the sixteen values of γ that were required to make Figure 4 converge. The parameters are identical to those used in Figure 3 but here no averaging of γ is performed. It is clear that the initial phase γ of the LP radiofrequency field at the moment of radical pair creation can have a significant effect on subsequent singlet-triplet mixing. By analogy with the discussion in the main

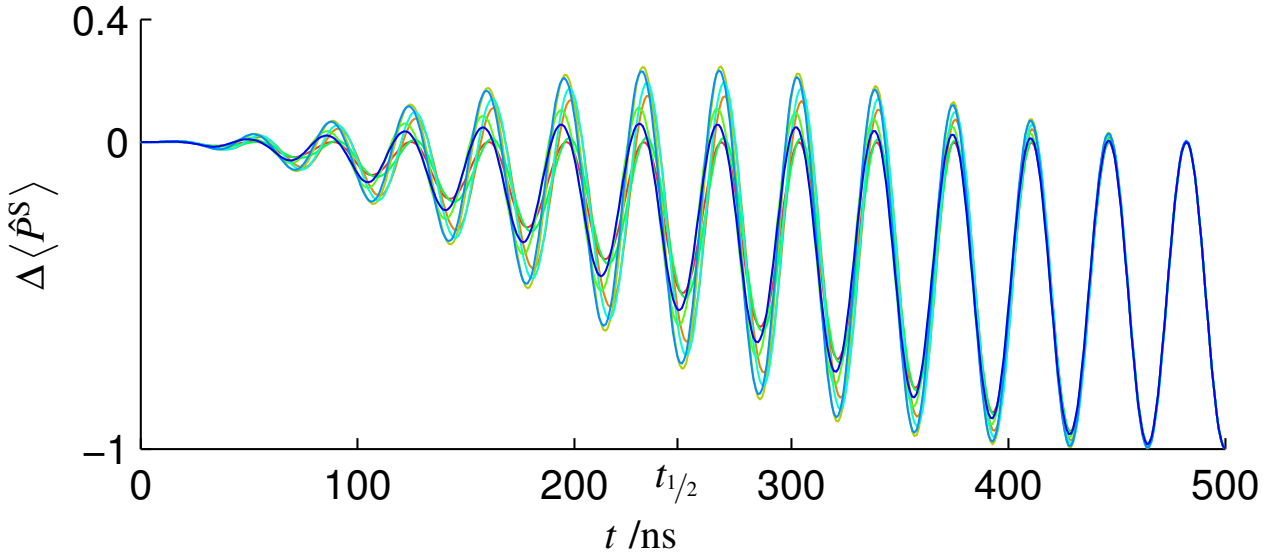

Figure S2: Simulations showing the changes in singlet probability caused by a LP radiofrequency field as a function of time. Calculations were performed using a Runge-Kutta (4,5) solver for radical pairs containing a single spin-½ nucleus. The graphs correspond to the simulations obtained using 16 equally spaced values of the intial RF phase $\gamma = 0, \pi/8, \ldots, 15\pi/8$. Other parameters: hyperfine coupling constant $a = 1.0\,\mathrm{mT}$, $B_1 = 100\,\mu\mathrm{T}$, $\nu_{\mathrm{rf}} = 28\,\mathrm{MHz}$, $k = 2.8 \times 10^6\,\mathrm{s}^{-1}$. The half-life of the radical pair (247 ns) is marked on the x-axis.

text, it is obvious that in order for these effects of initial RF phase γ to produce changes in the singlet product yield, the radical pair must have a sufficiently long lifetime so that significant differences in the spin evolution have time to develop. For this reason, the half-life of the radical pair used for the simulations is indicated on the x-axis of Figure S2.

Comparison with Figure 3 in the main paper shows that the differences between singlet probabilities arising from different initial RF phases γ is establihed earlier than the correspondingly large differences between CP and LP fields. In other words, the fact that RPs are created continuously in our experiments so that they do not have a well-definied initial RF phase γ, delays the onset of significant effects of RF polarization on singlet probability.

Finally, it is apparent that after $\sim 450\,\mathrm{ns}$, the singlet probabilities for different initial RF phases γ become very similar again. When the spin evolution is viewed over longer times, one observes a beating effect where the singlet probabilities for different initial RF phases γ alternate between being

similar, disparate and similar again.

S1.7 Time-dependent perturbation theory

In light of the slow, RF-field-strength-dependent onset of polarization effects, it seems natural to make a perturbation theory analysis. We present here the most fruitful of several such approaches that we attempted.

First, we separate the Hamiltonian for a one-proton radical pair into terms

$$\hat{H} = \hat{H}_0 + \hat{V}(t), \tag{S16}$$

where $\hat{H}_0 = a\hat{\boldsymbol{I}} \cdot \hat{\boldsymbol{S}}_\mathrm{A}$ does not depend on time and where

$$\hat{V}(t) = \begin{cases} \omega_1 \sqrt{2} \cos\left(\omega_\mathrm{rf} t + \gamma\right) \left(\hat{S}_{\mathrm{A}z} + \hat{S}_{\mathrm{B}z}\right) \\ \omega_1 \cos\left(\omega_\mathrm{rf} t + \gamma\right) \left(\hat{S}_{\mathrm{A}z} + \hat{S}_{\mathrm{B}z}\right) \pm \omega_1 \sin\left(\omega_\mathrm{rf} t + \gamma\right) \left(\hat{S}_{\mathrm{A}x} + \hat{S}_{\mathrm{B}x}\right) \end{cases} \tag{S17}$$

for linearly and circularly polarized RF respectively. Note that we have defined these fields in the xz-plane here, since this means that the Hamiltonian matrix is real, simplifying further analysis. We proceed by transforming into the interaction representation [10, 11], defining an interaction representation Hamiltonian $\hat{H}_\mathrm{I}(t)$ as

$$\hat{H}(t) \rightarrow \hat{H}_\mathrm{I}(t) = \hat{V}_\mathrm{I}(t) = \mathrm{e}^{\mathrm{i}\hat{H}_0 t} \hat{V}(t) \mathrm{e}^{-\mathrm{i}\hat{H}_0 t}. \tag{S18}$$

In order to remain consistent with the normal Schrödinger representation, all other operators transform as

$$\hat{\Omega}(t) \rightarrow \hat{\Omega}_\mathrm{I}(t) = \mathrm{e}^{\mathrm{i}\hat{H}_0 t} \hat{\Omega}(t) \mathrm{e}^{-\mathrm{i}\hat{H}_0 t} \tag{S19}$$

and the new basis states $|\psi_\mathrm{I}\rangle(t) = \mathrm{e}^{\mathrm{i}\hat{H}_0 t} |\psi\rangle$ evolve according to

$$\mathrm{i} \frac{\partial |\psi_\mathrm{I}\rangle(t)}{\partial t} = \hat{V}_\mathrm{I}(t) |\psi_\mathrm{I}\rangle(t) \tag{S20}$$

where $\hat{V}_\mathrm{I}(t)$ is measured in angular frequency units.

Now, since $\left|\hat{V}_\mathrm{I}(t)\right| = \left|\hat{V}(t)\right| \propto \omega_1$, the interaction representation Hamiltonian is "small" when the RF field is weak. We may therefore solve equation (S20) by iterative expansion into the following Neumann series:

$$|\psi_\mathrm{I}\rangle(t) = \left\{ 1 - \mathrm{i} \int_0^t \mathrm{d}t_1 \hat{V}_\mathrm{I}(t_1) - \int_0^t \mathrm{d}t_1 \int_0^{t_1} \mathrm{d}t_2 \hat{V}_\mathrm{I}(t_1) \hat{V}_\mathrm{I}(t_2) + \ldots \right\} |\psi_\mathrm{I}\rangle(0). \tag{S21}$$

For our purposes, it is most convenient to make calculations using the interaction representation den-

sity matrix

$$\hat{\rho}_{\mathrm{I}}(t) \equiv |\psi_{\mathrm{I}}\rangle(t)\langle\psi_{\mathrm{I}}|(t). \tag{S22}$$

Substituting the Neumann series from equation (S21) and collecting terms of the same order [2], we write

$$\hat{\rho}_{\mathrm{I}}(t) = \left\{1 - \mathrm{i}\int_0^t \mathrm{d}t_1 \hat{V}_{\mathrm{I}}(t_1) + \ldots\right\} |\psi_{\mathrm{I}}\rangle(0)\langle\psi_{\mathrm{I}}|(0) \left\{1 + \mathrm{i}\int_0^t \mathrm{d}t_1 \hat{V}_{\mathrm{I}}(t_1) + \ldots\right\} \tag{S23}$$

$$= \hat{\rho}(0) - \mathrm{i}\int_0^t \mathrm{d}t_1 \left[\hat{V}_{\mathrm{I}}(t_1), \hat{\rho}(0)\right] - \int_0^t \mathrm{d}t_1 \int_0^{t_1} \mathrm{d}t_2 \left[\hat{V}_{\mathrm{I}}(t_1), \left[\hat{V}_{\mathrm{I}}(t_2), \hat{\rho}(0)\right]\right] + \ldots \tag{S24}$$

This expression may be used to calculate contributions to the singlet probability

$$\left\langle \hat{P}^{\mathrm{S}} \right\rangle(t) = \mathrm{Tr}\left[\hat{P}^{\mathrm{S}}\hat{\rho}(t)\right] = \mathrm{Tr}\left[\hat{P}^{\mathrm{S}}_{\mathrm{I}}(t)\hat{\rho}_{\mathrm{I}}(t)\right]. \tag{S25}$$

We evaluated this expression with the aid of the symbolic manipulation program Mathematica. To first order, the singlet probability

$$\left\langle \hat{P}^{\mathrm{S}} \right\rangle(t) = \frac{5}{8} + \frac{3}{8}\cos at \tag{S26}$$

for both linearly and circularly polarized RF fields. In other words, the RF field does not have any first order effect on singlet probability in the one-proton radical pair. Continuing to second order, the singlet probability is given by an expression containing sines, cosines and powers of ω_{rf}, ω_1, a, t and γ. This expression is too bulky to give here, but the difference between RF polarizations is reasonably compact:

$$\left\langle \hat{P}^{\mathrm{S}} \right\rangle_{\mathrm{LP}} - \left\langle \hat{P}^{\mathrm{S}} \right\rangle_{\mathrm{CP}} = \frac{a\omega_1^2 \cos(\omega_{\mathrm{rf}} t + 2\gamma)}{8\left(\omega_{\mathrm{rf}}^3 - a^2\omega_{\mathrm{rf}}\right)^2} \times \begin{bmatrix} 3\omega_{\mathrm{rf}}^2 a - a^3 + \left(a^2 - \omega_{\mathrm{rf}}^2\right)\cos(\omega_{\mathrm{rf}} t)a \\ +\cos(at)\left(\omega_{\mathrm{rf}}^2 - a^2 + \left(a^2 - 3\omega_{\mathrm{rf}}^2\right)\cos(\omega_{\mathrm{rf}} t)\right)a \\ -2\omega_{\mathrm{rf}}^3 \sin(at)\sin(\omega_{\mathrm{rf}} t) \end{bmatrix}. \tag{S27}$$

It is clear that the second order contributions to the singlet probability produce a polarization effect that is proportional to ω_1^2 as we would expect.

However, if, as is necessary to model the experiments accurately, we average over the initial RF phase γ we find that

$$\frac{1}{2\pi}\int_0^{2\pi} \left\{\left\langle \hat{P}^{\mathrm{S}} \right\rangle_{\mathrm{LP}} - \left\langle \hat{P}^{\mathrm{S}} \right\rangle_{\mathrm{CP}}\right\} \mathrm{d}\gamma = 0. \tag{S28}$$

In other words, after averaging over the initial RF phase, LP and CP fields are equivalent even to second order. It is for this reason that RF fields of different polarization produce identical zero-field

EPR spectra in the limit of weak RF field strength and of rapid exponential-model decay.

S1.8 Propagators

It is possible to gain some insight into the significant coherent spin evolution by plotting propagators explicitly. Figure S3 shows the propagators in a one-proton radical pair for time intervals $t = 0 \rightarrow 3T/4$ and $t = 0 \rightarrow 30T$, where $T = 1/\nu_{\mathrm{rf}}$ is the period of the RF field, which is approximately 36 ns in this case. The plots are formed by first computing the requisite propagator, then subtracting a unit matrix in order to emphasise the coherent spin evolution and finally plotting the propagator as a group of squares whose side lengths are proportional to the absolute values of the corresponding elements. Propagators are plotted for spin evolution in CP$\pm$ and LP polarized fields.

After three quarters of an RF cycle, the figures in the left hand column show small, but significant differences in spin evolution under different RF polarizations. After 30 RF cycles, the figures on the right show marked differences. This is the same situation as we discussed in connection with Figure 4 of the main paper, where the singlet probabilities under different RF polarizations were initially similar but were then gradually seen to diverge. It should be noted that not all of these coherences are of direct relevance to the singlet probability. Only those coherences, highlighted with a grey box, that cause singlet–triplet interconversion directly affect the singlet probability.

Finally, it is apparent that despite giving identical singlet probabilities, CP+ and CP$-$ fields cause visibly different spin evolution. For example, one may compare Figures S3b and f. For a system whose Hamiltonian is given by equation (S2), we notice that when $\gamma = 0$ the difference between CP$\pm$ polarizations could be expressed by spin operator transformations: $\hat{S}_y \leftrightarrow -\hat{S}_y$ and $\hat{I}_y \leftrightarrow -\hat{I}_y$. Since there is no static field in that system, we could make the further transformation: $\hat{S}_z \leftrightarrow -\hat{S}_z$ and $\hat{I}_z \leftrightarrow -\hat{I}_z$ without any change to the Hamiltonian. Together, these transformations correspond to a "π_x pulse" — that is, to a certain relabelling of the basis states. Figures S3g and h plot the propagators for CP$-$ fields using a different order of basis states. These reordered plots are clearly identical to the CP+ ones above. This demonstrates graphically that CP$\pm$ fields produce different, but equivalent, spin evolution in the absence of a static field. Hence, they give rise to the same time-dependent singlet probability.

S2 Futher information on the experimental apparatus

A simple overall block diagram of the apparatus is shown in Figure S4, showing the various interconnections between the systems. Each of the subsystems will now be dealt with in more detail.

S2.1 Sample block

A bespoke square cross-section cuvette lies at the heart of the experiment, constructed from SUPRASIL® quartz, and with outer dimensions 5 mm $\times$ 5 mm $\times$ 15 mm, optical path length 3 mm. Short lengths of

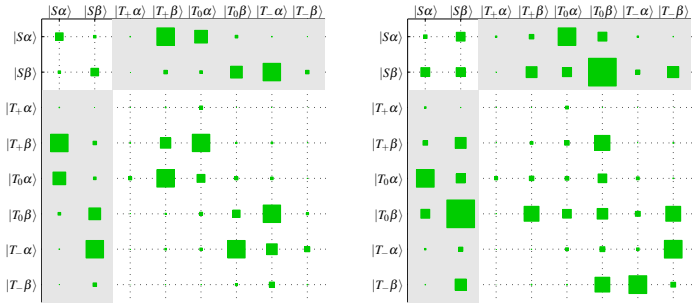

(a) CP−, $t = 3T/4$ (b) CP−, $t = 30T$

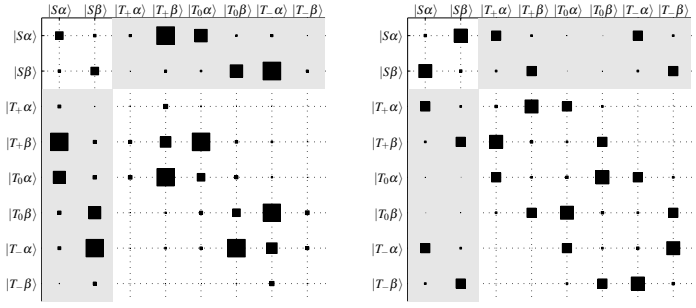

(c) LP, $t = 3T/4$ (d) LP, $t = 30T$

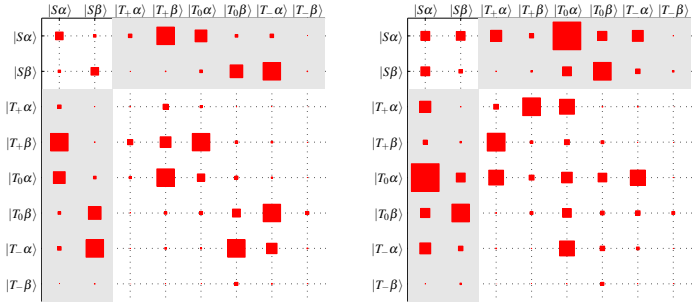

(e) CP+, $t = 3T/4$ (f) CP+, $t = 30T$

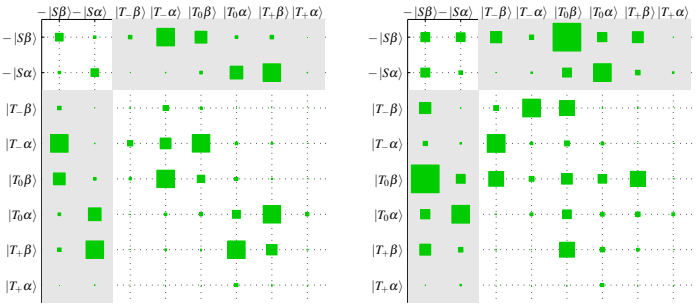

(g) Reordered basis CP−, $t = 3T/4$ (h) Reordered basis CP−, $t = 30T$

Figure S3: Propagators in a one-proton radical pair with $\nu_{\mathrm{rf}} = 28\,\mathrm{MHz}$, $B_1 = 100\,\mu\mathrm{T}$, $a = 1.0\,\mathrm{mT}$ and $B_0 = 0\,\mathrm{mT}$. The propagators are plotted using the electron S–T basis. Each square represents an element whose absolute value is proportional to the side length. In order to emphasize coherent evolution of states, we subtract an identity matrix from each propagator before plotting.

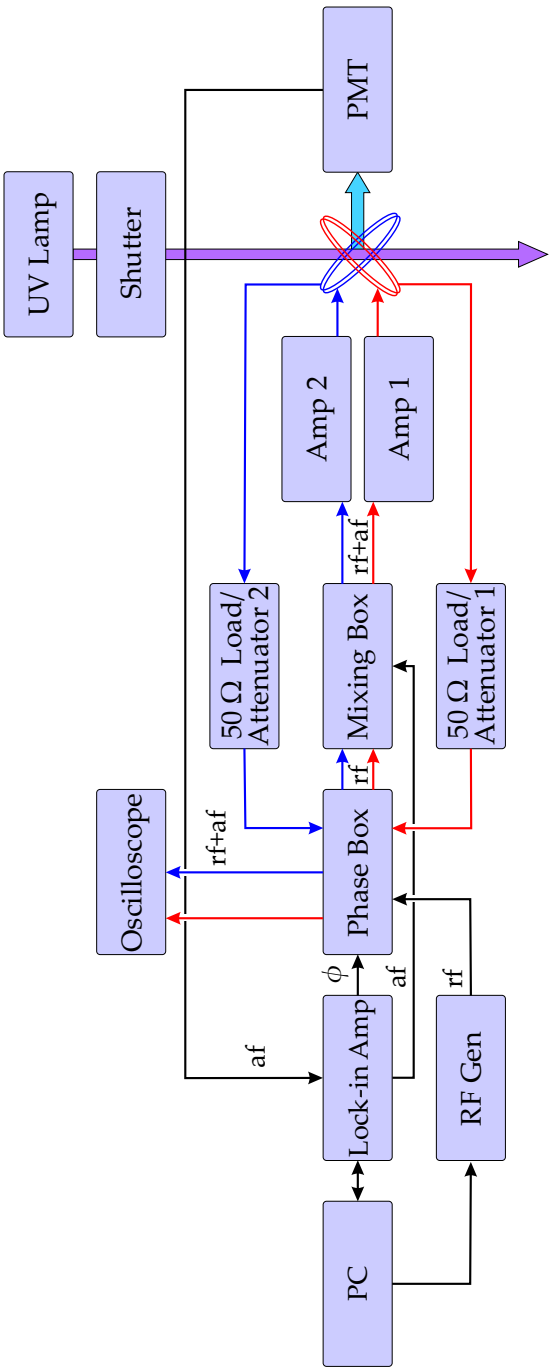

Figure S4: Block diagram of the experimental apparatus. Radiofrequency and audiofrequency signals are denoted 'rf' and 'af' respectively. The two separate radiofrequency channels and coils are shown coloured red and blue, and the phase-angle between them is ϕ. Detected magnetic-field-dependent exciplex emission, collected at 90° to the incident UV light is shown by the light blue arrow.

3 mm internal diameter glass tube fused to the two ends of the cuvette provide for the attachment of silicone tubing.

A two-piece machine-milled sample block was constructed from the plastic Delrin®. Tight-fitting square holes in both sections hold the cuvette securely in the correct position and orientation when the block is assembled. To the lid (shown in Figure S5) are clamped the two sets of radiofrequency coils, each consisting of two rectangular 12 mm × 5 mm loops of wire. The coils were connected to the cores of short lengths of coaxial cable, terminated at each end by BNC connectors. The two inputs were connected to the radiofrequency amplifiers, whilst the two outputs went to 50 Ω attenuators (see Section S2.4).

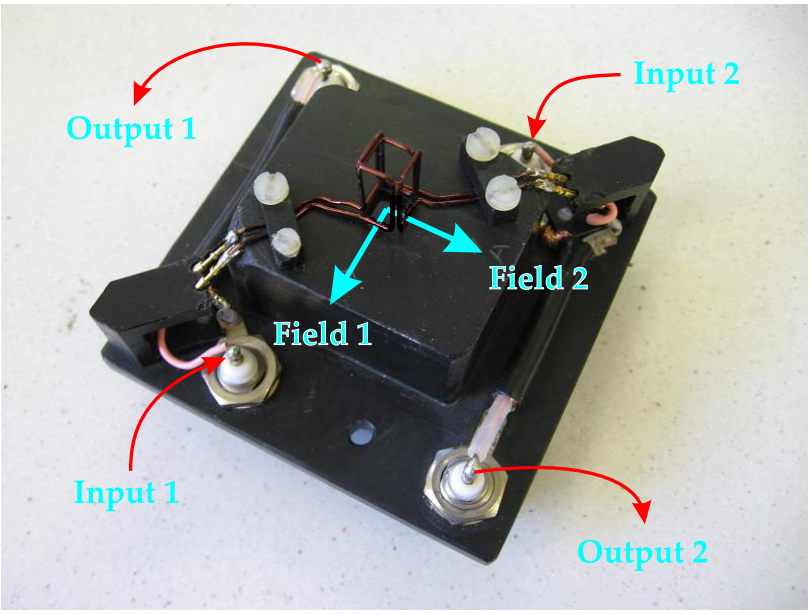

Figure S5: Photograph of the underside of the lid of the sample block showing the coils and BNC connections. The cuvette is supported between the coils by the lid and base of the block.

Two identical coil systems, mounted perpendicular to one another, allow the production of a LP or of either polarization of CP field by a simple ±90° radiofrequency phase shift. As Figure S6 shows, running the two channels in-phase produces an LP field, whilst introducing a phase shift of ±90° generates either left or right-handed polarization, the designation of which is arbitrary. In fact, both linear and circular polarizations may be thought of as special cases of an elliptically-polarized field.

The LP fields generated by each set of coils, $\boldsymbol{B}_1$ and $\boldsymbol{B}_2$ are given by:

$$\boldsymbol{B}_1 = \boldsymbol{i}' B_1 \cos(\omega_{\mathrm{rf}} t) \tag{S29}$$

$$\boldsymbol{B}_2 = \boldsymbol{j}' B_1 \cos(\omega_{\mathrm{rf}} t + \phi), \tag{S30}$$

where the phase shift of the second channel relative to the first is ϕ and the axes are determined by the orthonormal vectors $\boldsymbol{i}' = (\boldsymbol{i} + \boldsymbol{j})/\sqrt{2}$ and $\boldsymbol{j}' = (\boldsymbol{i} - \boldsymbol{j})/\sqrt{2}$.

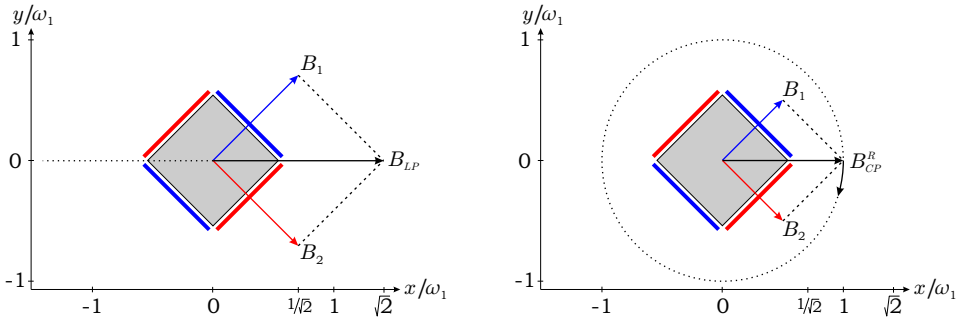

(a) LP field at $t = 0$ (b) CP field at $t = T/8$

Figure S6: Schematic of the sample, coils and fields as viewed from above. The sample cuvette is shaded grey and the two sets of coils are shown by red and blue bars; their field vectors are correspondingly colour-coded. The resultant fields are shown by black vectors. In (a) the LP field oscillates along $y = 0$, whilst in (b) the CP field follows a circle of radius ω_1 centred on the origin. Further explanation may be found in the text.

Thus for an LP field $\boldsymbol{B}_{\mathrm{LP}}$ with $\phi = 0$,

$$\boldsymbol{B}_{\mathrm{LP}} = (\boldsymbol{i}' + \boldsymbol{j}')B_1 \cos(\omega_{\mathrm{rf}} t) \tag{S31}$$

$$= \boldsymbol{i}\sqrt{2}B_1 \cos(\omega_{\mathrm{rf}} t), \tag{S32}$$

i.e. a field of amplitude $\sqrt{2}B_1$ directed along the x-axis, with an RMS magnitude of B_1. In contrast to this a field with a phase shift of $\phi = \mp\pi/2$ gives:

$$\boldsymbol{B}_{\mathrm{CP}\pm} = \boldsymbol{i}' B_1 \cos(\omega_{\mathrm{rf}} t) + \boldsymbol{j}' B_1 \cos(\omega_{\mathrm{rf}} t \mp \pi/2) \tag{S33}$$

$$= \boldsymbol{i}' B_1 \cos(\omega_{\mathrm{rf}} t) \pm \boldsymbol{j}' B_1 \sin(\omega_{\mathrm{rf}} t), \tag{S34}$$

which is a field of constant magnitude B_1 directed along $\boldsymbol{i}'$ at $t = 0$, and rotating anticlockwise (as viewed from above) with $\phi = +\pi/2$ and clockwise when $\phi = -\pi/2$.

Thus it can be seen that the oscillating fields produced via this method, with a simple phase shift, dissipate the same amount of power, and should give similar intensity effects. No μ-metal enclosure around the sample block was used, in contrast to the previous incarnation of the apparatus [12], as it was found that it created significant problems with radiofrequency pick-up. However, a μ-metal sheet was placed about 20 cm away from the sample to screen a weak static field emanating from the 19-inch rack-mount cabinet containing the radiofrequency equipment. The presence of this screening appeared to reduce any residual static field at the sample to $< 10\,\mu\mathrm{T}$, the lower limit of detection of the available Hall effect magnetic field probe. The mirror symmetry of the effect of the two circular polarizations obtained in calibration scans with a static field (shown below in Figure S8), and their similarity with zero applied field suggests that the residual static field had a negligible effect on the results presented here.

S2.2 Flow system

Solutions consisting of a 9:1 mix (by volume) of cyclohexanol and acetonitrile were made up with 10^{-3} M perdeuterated pyrene and 2×10^{-2} M 1,3-dicyanobenzene, as used in our previous experiments investigating static magnetic field effects [13].

The solutions were flowed to waste using a mechanical rack-and-pinion syringe driver. Rigid 3 mm internal diameter PTFE tubing was implemented as far as possible throughout the flow system, as the solvents employed degrade silicone and rubber-based pipes. However, short lengths of a minimally-deteriorating silicone hose had to be used to connect the ends of the inflexible and inelastic PTFE to the cuvette and syringe.

S2.3 Optical system

The sample was continuously illuminated by ultraviolet light from a Thermo-Oriel 6271 1000 W xenon-arc lamp, regulated by a Thermo-Oriel 69920 power supply which maintained constant power output. The majority of the focusing was accomplished with the strong lamp condenser lens close to the bulb; fine focusing was achieved with a 2.5 cm lens close to the sample block. Heating of the sample was prevented by removing the IR radiation through use of a 15 cm path-length water filter. After the IR filter, visible light was cut out with a pair of Oriel UG-5 250–400 nm short-pass filters, providing the correct wavelength (350 nm) for photolysis.

The design of the radiofrequency coils (see Figure S5) allowed perpendicular illumination and detection from the faces of the cuvette without obstructing the beam paths. A pair of 2.5 cm lenses focused the fluorescence, collected at 90° to the illumination beam, through an interference filter (centre 548 nm, 100 nm bandwidth, 90% peak transmission) onto the window of a photomultiplier tube (PMT). This was housed in a cylindrical μ-metal shield within a light-tight aluminium box, situated far from the coils (at a distance of 50 cm).

S2.4 Radiofrequency system

To allow both LP and CP oscillating fields to be investigated it was necessary to construct two matched radiofrequency circuits having the ability to phase-shift one by 90° relative to the other. The electronics inside the phase box are discussed separately in Section S2.5, but the rest of the radiofrequency system is explained here and shown in Figure S4.

A Programmed Test Sources PTS-500 frequency synthesizer, under computer control via its IEEE-488 (GPIB) interface, provides the radiofrequency signal with 0.1 Hz resolution; here the range 5 to 50 MHz was employed, running in steps of ~ 0.8 MHz. The output was applied to the radiofrequency input on the phase box (Section S2.5), which was effectively split into two channels, phase shifted if required, and subsequently multiplied by an audiofrequency modulation to allow for phase-sensitive detection (see Section S2.6). The outputs of these two channels were passed on to radiofrequency amplifiers.

The output of each radiofrequency amplifier (Kalmus 116FC-CE or Wessex Electronics RC114-100, both of which may provide 100 W RMS output), drives a low-inductance coil in series with a Bird Electronics 150 W 20 dB 50 Ω attenuator. Thus only a small proportion of the power is dissipated in an oscillating field at the sample, but the field strength should be reasonably constant across the frequency range of this broadband experiment. The outputs of the attenuators are then connected back into the phase box, providing a feedback loop to regulate the power provided by each channel. Two output channels on the phase box allow the returning signals from the attenuators to be monitored on an oscilloscope to check phase and power matching. The entire radiofrequency circuit is approximately matched to 50 Ω without the use of current transformers.

S2.5 Phase box

The most difficult technical condition required for this experiment to function correctly is the maintenance of constant phase shift and field strength across the radiofrequency spectrum of interest. If the phase shift drifts, or the field produced by either coil differs from that of the other, or if their fields are not perpendicular, then both LP and CP situations will become elliptically polarized and any polarization effect will decrease. A block diagram of the system which performs phase and power matching is given in Figure S7. A fuller description follows, but in essence, the radiofrequency generator signal is split into two channels which are mutually phase shifted, amplified and sent to the power amplifiers; on their return from the attenuators, the signals are compared to a reference for phase and power and appropriate feedback adjustments made to the system to correct for deviations from the expected values.

As Figure S7 shows, the phase modifications are actually applied in a subcircuit (blue connections) running at high radiofrequencies, as the components necessary to achieve this are much cheaper and more readily available than the corresponding parts for frequencies required in the experiment. Hence the 5 to 60 MHz reference signal is boosted by 200 MHz. This is achieved by measuring the phase and frequency of the generator signal, and using a voltage controlled oscillator to create a new, clean reference; a feedback loop stabilizes the output.

This signal is then split, and, for a phase shift of ϕ, the two signals are shifted $\pm\phi/2$ respectively. In the current configuration of the box, the phase may be altered continuously across the range $\pm 120^\circ$, but measurements are only taken at 0° and $\pm 90^\circ$. A computer-controlled voltage from the lock-in amplifier (see Section S2.6) adjusts the shift, which was found to have a slight frequency dependence — a calibration curve (not shown) was constructed and applied in custom written LabVIEW control software to ensure stability.

After the phase shift, multiplication by the 200 MHz reference and application of a low pass filter on each channel down-shifts the frequency to the required range to send to the radiofrequency power amplifiers.

Passing round the circuit, through the coils and attenuators, the channels then return to the phase box, at which point they are compared to the incoming radiofrequency generator signal at a sample

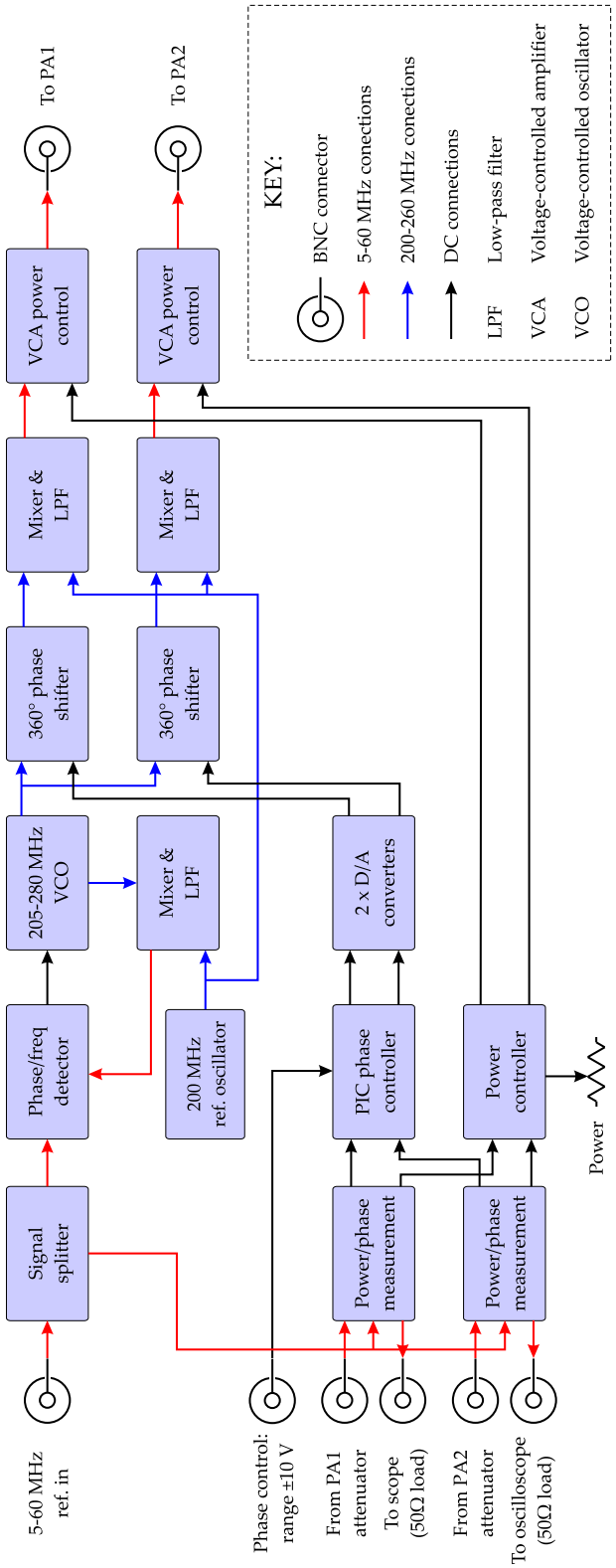

Figure S7: Block diagram of the phase box, showing that the reference frequency is boosted by 200 MHz to allow the use of cheaper components. Each channel is controlled independently and compared to the reference to maintain power output across the 5-80 MHz frequency range.

rate of 2 kHz using Analog Devices AD8302 integrated circuits. These provide phase and frequency information compared to the reference in two output DC voltages for each channel.

A 16F874 PIC microcontroller is used to determine the slope of the AD8302 phase outputs on each channel and control the phase via digital-to-analgoue converters and feedback through voltage-controlled 360° phase shifters. Output power is manipulated by simple analogue difference-amplifiers and radiofrequency voltage-controlled amplifiers.

In this way, both channels are compared to a single reference signal in real-time, giving independent power control for each channel and a relative mutual phase control. The PTS500 produces a high-quality reference signal of constant amplitude across the range of interest; thus the system should be robust to power discrepancies caused by having non-matched amplifiers, by adjusting the input to whichever amplifier strays from the correct power. All experiments are run at the same root-mean-square power, whether LP or CP; the amplifiers produce the same power in each case — the only difference between the two is the phase shift.

Integral to the success of phase and power matching is that the signal paths are identical on the two channels: the coils must produce the same fields given identical inputs; the attenuators must reduce the signal by the same degree; all cables must be identical lengths so as not to introduce a spurious phase shift. Tests were carried out to ensure that swapping channels and components had no effect on the signals recorded. As further reassurance, reaction-yield detected magnetic resonance (RYDMR) spectra were recorded. The RYDMR experiment records the exciplex fluorescence as a function of static field strength in the presence of a radiofrequency field of fixed frequency and strength. The resulting spectra are presented in Figure S8. There is a very clear symmetry about the y-axis in this figure. This shows that when on-resonance, both polarizations of CP field affect $\mathsf{S} \leftrightarrow \mathsf{T}$ mixing identically; the polarization that shows a Zeeman resonance depends only on the sense of the applied static field. These results also demonstrate that the effect of a LP field does not depend upon the static field polarity.

S2.6 Phase-sensitive detection

Phase-sensitive detection was used to enhance dramatically the sensitivity of the apparatus. Its application for the oscillating fields used here was technically more difficult than simply modulating a static field as previously [13]; while the introduction of an audiofrequency modulation envelope on top of a radiofrequency oscillation is relatively easy, overcoming its effect on the stability of the phase box output had to be achieved by slowing the response of the system to a point where the modulation appeared fast on this timescale. The observed signal is given by the difference in fluorescence upon application of the oscillating field (relative to applying no oscillating field). The dual-channel, digital lock-in amplifier (Stanford Research Systems SRS830) is employed here as the phase-sensitive detector.

100%-amplitude modulation of the radiofrequency is introduced at 381 Hz. Once initial modifications were made to the phase box, this did not appear to upset phase and power matching, as

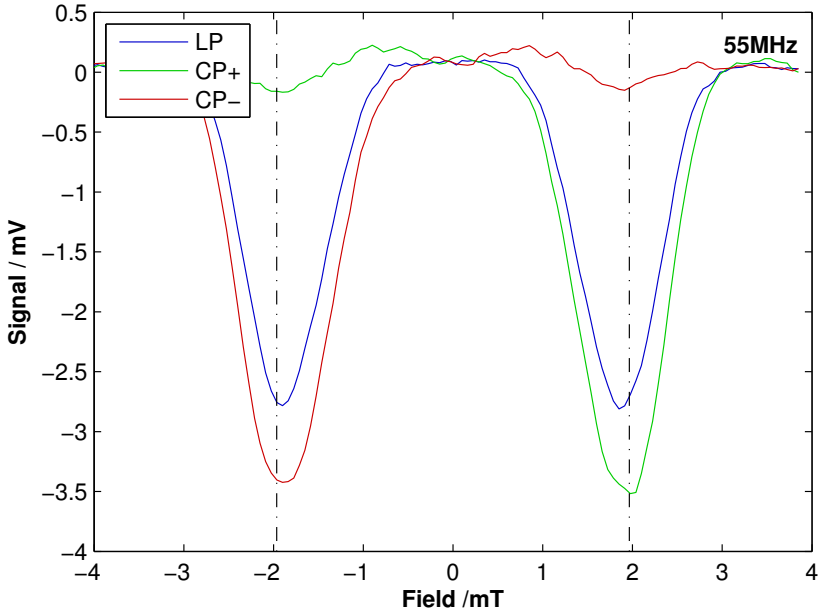

Figure S8: 55 MHz field-swept experiment with chrysene$_{h12}$ + 1,2-dicyanobenzene. Under application of both static and perfectly polarized radiofrequency fields, the two CP fields should give mirror-image spectra.

monitored on the oscilloscope outputs.

S2.7 Suppression of radiofrequency interference

The experiment involves high-power radiofrequency, with peak-to-peak voltages up to 300 V and currents of several amperes in some components [12]. Imperfect contacts may allow spurious signals to arise within equipment, while the combined lengths of leads are of the order of the radiofrequency wavelengths used, allowing cabling to behave as an active transmitter or antenna. Ground loops, caused when equipment is earthed through two separate connections (such as its mains plug and then via a signal lead to another earthed box), may also introduce unwanted pick-up. To avoid all these problems, careful consideration must be paid to the arrangement and connection of apparatus and the course of cables.

In a bid to reduce interference, all connections between apparatus were made with high-quality double-screened coaxial cable. All radiofrequency equipment was housed in a 19-inch rack-mount cabinet, so that the only electronic items outside this enclosure were the coils, the wires to and from the sample block, the photomultiplier tube and its power supply unit, and the lock-in amplifier. Within the cabinet, all equipment cases were earthed to a single point, and whilst ‘dirty’ mains power was supplied to the equipment in the cabinet, a ‘clean’ mains supply fed the photomultiplier tube and lock-in amplifier.

The arc lamp power supply unit, its electromechanical shutter and the computer were connected to a third electricity supply, and the lamp power supply unit was moved as far from the radiofrequency

sources as possible. Clamp-on cable ferrite chokes were attached to cables and mains leads which carried no radiofrequency signals.

Background scans, taken with a solution containing only pyrene, which should have no magnetic field-dependence, readily highlighted any pick-up. While the phase box has the potential to run up to $\sim 80\,\mathrm{MHz}$, particularly troublesome interference above 60 MHz, coupled with a paucity of magnetic effects at these frequencies, led to data only being collected in the range 5 to 50 MHz.

A Details of rotating frame transformation

A.1 Product operator rules

In order to find the rotating frame Hamiltonian, we evaluate equation (S6), taking each term in the full Hamiltonian separately. First, however, we note a few useful identities for a general spin $\hat{\boldsymbol{L}}$ under a unitary transformation $U = \exp\left(\mathrm{i}\theta\hat{L}_z\right)$:

$$\begin{aligned} U\hat{L}_x U^\dagger &= \hat{L}_x\cos\theta - \hat{L}_y\sin\theta \\ U\hat{L}_y U^\dagger &= \hat{L}_x\sin\theta + \hat{L}_y\cos\theta \\ U\hat{L}_z U^\dagger &= \hat{L}_z. \end{aligned} \tag{S35}$$

A.2 Hyperfine term

Applying these rules to the hyperfine term, $\hat{\boldsymbol{I}}_{Ni}\cdot\hat{\boldsymbol{S}}_N$, gives a contribution

$$\begin{aligned} &T(t)\left(\hat{\boldsymbol{I}}_{Ni}\cdot\hat{\boldsymbol{S}}_N\right)T^\dagger(t) \\ &\quad= \left[\exp\left(\mathrm{i}\hat{I}_{Niz}\omega_{\mathrm{rf}}t\right)\hat{\boldsymbol{I}}_{Ni}\exp\left(-\mathrm{i}\hat{I}_{Niz}\omega_{\mathrm{rf}}t\right)\right]\cdot\left[\exp\left(\mathrm{i}\hat{S}_{Nz}\omega_{\mathrm{rf}}t\right)\hat{\boldsymbol{S}}_N\exp\left(-\mathrm{i}\hat{S}_{Nz}\omega_{\mathrm{rf}}t\right)\right] \\ &\quad= \left[\hat{I}_{Nix}\cos\omega_{\mathrm{rf}}t - \hat{I}_{Niy}\sin\omega_{\mathrm{rf}}t\right]\left[\hat{S}_{Nx}\cos\omega_{\mathrm{rf}}t - \hat{S}_{Ny}\sin\omega_{\mathrm{rf}}t\right] \\ &\qquad+ \left[\hat{I}_{Nix}\sin\omega_{\mathrm{rf}}t + \hat{I}_{Niy}\cos\omega_{\mathrm{rf}}t\right]\left[\hat{S}_{Nx}\sin\omega_{\mathrm{rf}}t + \hat{S}_{Ny}\cos\omega_{\mathrm{rf}}t\right] + \hat{I}_{Niz}\hat{S}_{Nz} \\ &\quad= \hat{\boldsymbol{I}}_{Ni}\cdot\hat{\boldsymbol{S}}_N. \end{aligned} \tag{S36}$$

In other words, the hyperfine term is unaffected by the RFT. Note that this is only the case when the hyperfine tensor is isotropic, or when it has axiality directed along the axis of rotation of the RF field.

A.3 Static field term

When the static field is oriented along the axis of rotation of the RF field, it makes a contribution of $\omega_0\hat{S}_{Nz}$ to both the full and rotating frame Hamiltonians. For other orientations the rotating frame Hamiltonian would become time-dependent, and therefore cease to be useful.

A.4 RF field term

The RF field term makes a contribution proportional to

$$T(t)\left[\left(\hat{S}_{Nx}-\hat{S}_{Ny}\right)\cos\left(\omega_{\mathrm{rf}}t+\gamma\right)+\left(\hat{S}_{Nx}+\hat{S}_{Ny}\right)\sin\left(\omega_{\mathrm{rf}}t+\gamma\right)\right]T^{\dagger}(t)$$
$$=\hat{S}_{Nx}\left(\cos\gamma+\sin\gamma\right)+\hat{S}_{Ny}\left(\sin\gamma-\cos\gamma\right). \tag{S37}$$

In other words, the RF field makes a contribution to the rotating frame Hamiltonian as if it were a static field with the same strength, oriented along the direction that the RF field has instantaneously at $t=0$ in the laboratory frame. Since there is axial symmetry about the z-axis for the RP systems that we consider, γ is irrelevant and we may choose our coordinate system such that $\gamma=\pi/4$ for convenience. There is therefore no need to average over γ when the RFT is applicable.

A.5 "Coriolis" term

The term $\mathrm{i}\frac{\partial T(t)}{\partial t}T^{\dagger}(t)$ is an additional contribution that arises in the rotating frame Hamiltonian as a side-effect of the time dependence of the transformed basis states. It is analogous to the Coriolis "force" that must be included when working in a non-inertial reference frame in classical mechanics [14]. Using the definition of $T(t)$ in equation (S8), we write

$$\mathrm{i}\frac{\partial T(t)}{\partial t}T^{\dagger}(t)=\mathrm{i}\sum_i \mathrm{i}\hat{L}_{iz}\omega_{\mathrm{rf}}T(t)T^{\dagger}(t)=-\omega_{\mathrm{rf}}\sum_i\hat{L}_{iz}. \tag{S38}$$

This term is almost equivalent to the Zeeman interaction with a fictitious magnetic field along the $-z$-axis. The only quirk with this interpretation is that the field appears to have strength $B_1^{\mathrm{eff}}=\omega_{\mathrm{rf}}/\gamma_{\mathrm{e}}$ to the electrons but it must appear much stronger ($B_1^{\mathrm{eff}}=\omega_{\mathrm{rf}}/\gamma_{\mathrm{n}}$) to the nuclei in order that both electron and nuclear spins precess at the same frequency.

A.6 Liouville–von Neumann equation

Thus far, we have shown how a clever choice of basis states transforms the Hamiltonian of a RP in the presence of a circularly polarized RF field into a time-independent rotating frame Hamiltonian $\hat{H}'$. In terms of these new basis states, the wave function of the RP evolves according to the normal time-dependent Schrödinger equation with the $\hat{H}'$ replacing the Hamiltonian.

Now, in order to calculate magnetic field effects, we frequently need to treat systems that are not found in a pure state. For example, we normally consider that there is negligible nuclear spin polarization at the instant of RP creation and therefore consider an ensemble of RPs with all possible nuclear spin states. This is most easily done by using the density matrix formalism. A system is described by its density matrix

$$\hat{\rho}(t)=|\psi\rangle(t)\langle\psi|(t) \tag{S39}$$

which evolves under the action of the Liouville–von Neumann equation

$$\frac{\partial \hat{\rho}(t)}{\partial t} = -\mathrm{i}\left[\hat{H}(t), \hat{\rho}(t)\right]. \tag{S40}$$

The expectation value of an operator $\hat{\Omega}$ is given by

$$\left\langle \hat{\Omega} \right\rangle (t) = \mathrm{Tr}\left[\hat{\Omega}\hat{\rho}(t)\right]. \tag{S41}$$

Making the transformation to the rotating frame, we find that the system may also be described by its rotating frame density matrix

$$\hat{\rho}'(t) = |\phi\rangle(t)\langle\phi|(t) = T(t)\hat{\rho}(t)T^{\dagger}(t) \tag{S42}$$

which evolves under the action of the Liouville–von Neumann equation

$$\frac{\partial \hat{\rho}'(t)}{\partial t} = -\mathrm{i}\left[\hat{H}'(t), \hat{\rho}'(t)\right]. \tag{S43}$$

The expectation value of an operator $\hat{\Omega}$ is given by

$$\left\langle \hat{\Omega} \right\rangle (t) = \mathrm{Tr}\left[\hat{\Omega}\hat{\rho}(t)\right] = \mathrm{Tr}\left[\hat{\Omega}T^{\dagger}(t)T(t)\hat{\rho}(t)T^{\dagger}(t)T(t)\right] \tag{S44}$$

which by cyclic permutation of the trace gives

$$\left\langle \hat{\Omega} \right\rangle (t) = \mathrm{Tr}\left[T(t)\hat{\Omega}T^{\dagger}(t)T(t)\hat{\rho}(t)T^{\dagger}(t)\right] = \mathrm{Tr}\left[\hat{\Omega}'\hat{\rho}'(t)\right]. \tag{S45}$$

A.7 Singlet projection operator

In order to calculate RP singlet probabilities in the rotating frame it remains only to consider the form of the singlet projection operator, $\hat{P}^{\mathrm{S}} = \frac{1}{4} - \hat{\boldsymbol{S}}_{\mathrm{A}} \cdot \hat{\boldsymbol{S}}_{\mathrm{B}}$, as we transform to the rotating frame. Applying equation (S35) gives

$$\begin{aligned}
&T(t)\left(\frac{1}{4} - \hat{\boldsymbol{S}}_{\mathrm{A}} \cdot \hat{\boldsymbol{S}}_{\mathrm{B}}\right)T^{\dagger}(t) \\
&= \frac{1}{4} - \left[\exp\left(\mathrm{i}\hat{S}_{\mathrm{A}z}\omega_{\mathrm{rf}}t\right)\hat{\boldsymbol{S}}_{\mathrm{A}}\exp\left(-\mathrm{i}\hat{S}_{\mathrm{A}z}\omega_{\mathrm{rf}}t\right)\right] \cdot \left[\exp\left(\mathrm{i}\hat{S}_{\mathrm{B}z}\omega_{\mathrm{rf}}t\right)\hat{\boldsymbol{S}}_{\mathrm{B}}\exp\left(-\mathrm{i}\hat{S}_{\mathrm{B}z}\omega_{\mathrm{rf}}t\right)\right] \\
&= \frac{1}{4} - \left[\hat{S}_{\mathrm{A}x}\cos\omega_{\mathrm{rf}}t - \hat{S}_{\mathrm{A}y}\sin\omega_{\mathrm{rf}}t\right]\left[\hat{S}_{\mathrm{B}x}\cos\omega_{\mathrm{rf}}t - \hat{S}_{\mathrm{B}y}\sin\omega_{\mathrm{rf}}t\right] \\
&\quad - \left[\hat{S}_{\mathrm{A}x}\sin\omega_{\mathrm{rf}}t + \hat{S}_{\mathrm{A}y}\cos\omega_{\mathrm{rf}}t\right]\left[\hat{S}_{\mathrm{B}x}\sin\omega_{\mathrm{rf}}t + \hat{S}_{\mathrm{B}y}\cos\omega_{\mathrm{rf}}t\right] - \hat{S}_{\mathrm{A}z}\hat{S}_{\mathrm{B}z} \\
&= \frac{1}{4} - \hat{\boldsymbol{S}}_{\mathrm{A}} \cdot \hat{\boldsymbol{S}}_{\mathrm{B}}.
\end{aligned} \tag{S46}$$

In other words, the singlet projection operator is unaffected by the RFT. The same result also holds for the triplet projection operator.

A.8 Summary

The derivation above is for CP+ RF fields ($\phi_{\mathrm{rf}} = +\pi/2$) which rotate in the same sense as the Larmor precession. CP− RF fields may be treated in the same manner. The CP− Hamiltonian may also be obtained by symmetry, replacing $\omega_0 \rightarrow -\omega_0$ in the Hamiltonian.

Combining these results, the rotating frame Hamiltonian for a system subject to a CP± field is

$$\hat{H}' = \sum_{N=\mathrm{A}}^{\mathrm{B}} \left(\pm\omega_0 - \omega_{\mathrm{rf}}\right)\hat{S}_{Nz} + \omega_1 \hat{S}_{Nx} + \sum_i \left\{ a_{Ni}\,\hat{\boldsymbol{I}}_{Ni} \cdot \hat{\boldsymbol{S}}_N - \omega_{\mathrm{rf}} \hat{I}_{iz} \right\}. \tag{S47}$$

In such systems, the rotating frame Hamiltonian given here is exact. This Hamiltonian is time-independent and contains no interactions between the two radicals; it is of the form $\hat{H} = \hat{H}^{\mathrm{A}} + \hat{H}^{\mathrm{B}}$. Hence, singlet yields may be calculated very efficiently.

In radical pairs with non-axial hyperfine interactions, or where the hyperfine axiality is not along the RF axis, or when the RF field is not circularly polarized, or when there is a static field that is not along the RF axis, the rotating frame Hamiltonian is time-dependent. In such situations, the RFT provides no benefit for an exact calculation.

References

[1] M. H. Levitt. *Spin Dynamics: Basics of Nuclear Magnetic Resonance*. Wiley, 2001.

[2] C. P. Slichter. *Principles of Magnetic Resonance*. Springer-Verlag, 3rd edition, 1990.

[3] J. M. Canfield, R. L. Belford, P. G. Debrunner, and K. Schulten. A perturbation theory treatment of oscillating magnetic fields in the radical pair mechanism. *Chem. Phys.*, 182:1–18, 1994.

[4] I. I. Rabi, N. F. Ramsey, and J. Schwinger. Use of rotating coordinates in magnetic resonance problems. *Rev. Mod. Phys.*, 26(2):167–171, 1954.

[5] R. K. Wangsness and F. Bloch. The dynamical theory of nuclear induction. *Phys. Rev.*, 89(4):728–739, 1954.

[6] F. Bloch. Dynamical theory of nuclear induction. II. *Phys. Rev.*, 102(1):104–135, 1956.

[7] F. Bloch. Nuclear induction. *Phys. Rev.*, 70(7–8):460–474, 1946.

[8] F. Bloch and A. Siegert. Magnetic resonance for nonrotating fields. *Phys. Rev.*, 57(6):522–527, 1940.

[9] J. Schwinger. On nonadiabatic processes in inhomogeneous fields. *Phys. Rev.*, 51(8):648–651, 1937.

[10] C. Cohen-Tannoudji. *Quantum Mechanics*. John Wiley & Sons Inc, 1977.

[11] A. S. Davydov. *Quantum Mechanics*. International series in Natural Philosophy. Pergamon Press, 2nd edition, 1976.

[12] C. R. Timmel, J. R. Woodward, P. J. Hore, K. A. McLauchlan, and D. V. Stass. A zero-field electron spin resonance spectrometer for the study of transient radical ion pairs. *Meas. Sci. Tech.*, 12:635–643, 2001.

[13] C. T. Rodgers, S. A. Norman, K. B. Henbest, C. R. Timmel, and P. J. Hore. Determination of Radical Re-encounter Probability Distributions from Magnetic Field Effects on Reaction Yields. *J. Am. Chem. Soc.*, 129:6746–6755, 2007.

[14] T. W. B. Kibble and F. H. Berkshire. *Classical Mechanics*. Imperial College Press, 5th edition, 2004.